

Crystallography of Interfaces and Grain Size Distributions in Sr-Doped LaMnO₃

Qinyuan Liu,[§] Sudip Bhattacharya,^{§,¶,‡} Lam Helmick,^{§,¶} Sean P. Donegan,[§] Anthony D. Rollett,[§] Gregory S. Rohrer,[§] and Paul A. Salvador^{§,¶,†}

[§]Department of Materials Science and Engineering, Carnegie Mellon University, Pittsburgh, Pennsylvania 15213

[¶]National Energy Technology Laboratory (NETL), Morgantown, West Virginia 26507

Grain-boundary plane distributions (GBPDs), grain size distribution (GSDs), and upper tail departure from log-normal GSDs were quantified in dense and porous La_{0.8}Sr_{0.2}MnO₃ samples to understand expected microstructures in solid oxide fuel cells. Samples were sintered at 1450°C for 4 h and then annealed between 800°C and 1450°C. The GBPDs and normalized GSDs reached steady state during sintering and little variation occurred during annealing. The GBPDs were nearly isotropic, with the relative areas of {001} planes being slightly higher than random (and the relative areas of {111} planes being less than random). The porous sample had an almost identical GBPD, whereas the almost isotropic pore boundary plane distribution was essentially opposite to the GBPD. The upper tails of the experimental GSDs, and several theoretical distributions, were characterized using peaks-over-threshold analysis. Dense samples, and all normal grain growth models, exhibit lower frequencies of large grains in the upper tail than would a log-normal distribution, and the experimental distributions are similar to the Mullins distribution. Porous samples, however, have an anomalous increased frequency of large grains in the upper tail, as compared to all the model distributions, even though other metrics of the microstructure indicate the dense and porous systems are similar.

I. Introduction

HIGH-TEMPERATURE solid oxide fuel cells (SOFCs) offer highly efficient, clean, direct conversion of chemical to electrical energy.¹ SOFC performance is dictated by the activity and useable lifetime of the cell components. Benchmark cathodes are three-phase systems composed of an electron-conductor, an oxide ion conductor, and pores for gas diffusion.¹ The correlation between long-term SOFC performance and cathode microstructure evolution has already been demonstrated, primarily implicating grain coarsening, redistribution of phases, and formation of resistive secondary phases at the triple phase boundaries (TPBs).^{2–14} These changes are also manifest in the quantitative features of the microstructure,^{4,5,8,11–15} many of which we are only beginning to quantify experimentally^{14,16–23} or model computationally.²⁴ Using three-dimensional (3D) reconstructions of model systems, the total length of active TPBs were isolated as the key parameter that controls cathode activity.^{14,16–21} Complete 3D descriptions of the crystallographic nature of

microstructural features have been also obtained on small regions of SOFCs,²² as well as on dense yttria-stabilized zirconia (YSZ).²³ Such observations provide critical foundational information on the driving forces of long-term microstructural evolution in cathode systems, but are not available for most SOFC component materials. Toward this end, we report here on the crystallographic nature of grain and pore boundaries in dense and porous ceramics of La_{0.8}Sr_{0.2}MnO_{3±δ} (LSM-8020 or LSM herein), as well as detailed analyses of grain size distributions (GSDs).

The grain-boundary character distribution (GBCD) is the five parameter description of the relative areas of grain boundaries, based on three lattice misorientation parameters and two grain-boundary plane orientation parameters.^{25–27} GBCDs of polycrystalline ceramic materials,^{26,28–34} including YSZ,²³ have been measured using electron backscatter diffraction (EBSD), in which tens of thousands of grain-boundary segments were characterized. The GBCD is inversely related to the grain-boundary energy distribution (GBED), which drives microstructural evolution of a system.^{35–39} Considering baseline degradation mode in SOFCs to be grain coarsening by normal grain growth (for which mechanisms and kinetics can be well-described^{40–45}), little is known quantitatively about the expected evolution based on grain-boundary characteristics. In porous systems, the effects of the pore-boundary plane distributions (PBCDs), which describe the pore surface crystallography, must also be considered. A few studies have uncovered effects of surface crystallographic features on cathode surface properties,^{46,47} and others have quantified such crystallographic features in actual cathodes,^{22,33} but there are not enough observations to build strong correlations between crystallographic features and the evolution of cathode performance. This work serves as further initial investigations into the quantitative microstructural features of cathode systems in their initial states, quantifying the GBCDs and PBCDs for LSM-8020 ceramics.

The GSD is another important metric that captures information about microstructural evolution. Most ceramics exhibit GSDs that compare favorably to the log-normal distribution,^{44,48,49} but such comparisons are typically based on limited data or histograms that focus on the data in the vicinity of the mean.^{50,51} However, it is not clear whether cathode degradation is correlated to average microstructural features or deviations from the average. Other important material properties, such as creep and fatigue, are significantly influenced by a few large grains, considered outliers from the average and existing only in the upper-tail of the GSD.^{52–54} Here, we investigate the deviations from log-normality in dense and porous LSM, highlighting the effects of pores on increasing the deviation of the GSD from log-normal behavior, resulting in a statistical overpopulation of very large grains as compared to the log-normal behavior.

In one of the earliest analyses of grain growth by Hillert,⁵⁵ an equation was derived to predict the grain growth rate and

J. Blendell—contributing editor

Manuscript No. 34286. Received December 19, 2013; approved April 3, 2014.

[‡]Present Address: North American Höganäs, Inc., 111 Höganäs Way, Hollsopple, PA 15935

[†]Author to whom correspondence should be addressed. e-mail: paulsalvador@cmu.edu

GSD in single phase materials based on a classical LSW coarsening theory.^{56,57} Later, Mullins⁵⁸ analyzed the kinetics of grain growth based on a uniform boundary model (grain growth driven by self-similar curvature in two dimensions), which led to a GSD closer to those commonly observed (which deviate slightly from log-normal). Until recently,^{50,51} deviations of the GSD from log-normality have not been investigated in almost any polycrystalline material. An upper tail skewed toward few (more) large grains in the true GSD results in an over-sampling (under-sampling) of large grains if models using log-normal GSD are assumed. Thus, the misrepresentation of GSD tails could lead to inaccurate prediction of materials properties.⁵⁰ Tucker *et al.*⁵¹ investigated tail departure from a log-normal GSD from 3D microstructural reconstructions of nickel-based superalloys. They showed that the log-normal distribution did not fit either the upper or lower tails. Donegan *et al.*⁵⁰ used a peaks-over-threshold (POT) analysis to quantify the differences in the upper tails. This study reports the first analysis on the upper tail departure in the GSD of LSM-8020, using the POT analysis, and compares these to the Hillert,⁵⁵ Mullins,⁵⁸ and two-dimensional (2D) Potts⁵⁹ computational models.

LSM is an important cathode material owing to its high electronic conductivity, high electrochemical activity for oxygen reduction reaction, high thermal stability (both microstructural and long-term performance), and compatibility with common SOFC electrolytes (YSZ).^{1,60} LSM-8020 is a commonly investigated ceramic model of SOFC cathodes, though real cathode systems are typically A-site deficient, and may contain other cations to further modify baseline properties.^{1,60} Herein, dense and porous LSM-8020 samples (exposed to different processing conditions) were investigated to determine the GBCDs, the PBPDs, and GSDs.

II. Experimental Procedure

(1) Sample Preparation

Dense and porous LSM-8020 samples were prepared via tape casting⁶¹ using commercial SOFC cathode powders (LSM20-P, having particle sizes ranging from 300 to 700 nm) obtained from NexTech Materials (Lewis Center, OH). The slurry formulation [adapted from Ref. (61)] used for dense samples was modified with the addition of rice starch for the fabrication of porous samples, with a targeted porosity of 20%–30% by volume. Slurries were cast into 127 mm high tapes, dried, and punched to form cylindrical coupons. To form as-sintered (AS) samples, 12–16 coupons were uniaxially pressed together and sintered at 1450°C for 4 h (typical SOFC annealing conditions^{62,63}). Various AS samples were individually annealed for longer times and at different temperatures: 672 h at 800°C, 100 h at 1250°C, and 100 h at 1450°C. Hereafter the samples will be referred to as the AS, 800, 1250, and 1450 samples. Specimens for EBSD analysis were prepared by polishing with 0.02 μm colloidal slurry to obtain flat and scratch free surfaces and further annealed at 1000°C for 1 h to remove any defects and organic residues. Further details on sample preparation are given elsewhere.⁶⁴

(2) EBSD Data Collection and Processing

Orientation mapping was performed as described in detail elsewhere [see Refs. (23,64)]. Briefly, an environmental SEM (Quanta 200, FEI, Hillsboro, OR) operated at 25 keV was used to register EBSD patterns at a grid spacing of 0.25 μm . The local orientation at each point was assigned through automated analysis of EBSD patterns by TSL OIM™ software (version 7.0.1 \times 64, EDAX, Mahwah, NJ), assuming that LSM adopted a cubic perovskite structure. Multiple orientation maps for both dense and porous LSM specimens were collected and merged to generate sufficient observations for statistical analysis. The EBSD data were further

processed using the OIM™ software to reassign poorly indexed points near grain boundaries to grains, to average the orientation within any grain, to remove all points not associated with grains or whose orientation assignments had high uncertainties, and to reconstruct the grain boundaries [as described in Refs. (23,64)]. This procedure removed the erroneously indexed points inside pores and accurately captured the grain microstructure.

Inverse pole figure (IPF) maps, which show the surface orientation at each point with respect to the normal of the specimen surface, were also generated using the OIM™ software. The average grain diameter (determined from the grain area reported as the diameter of a circle of equivalent area) and GSDs were determined from at least 6800 grains. The reconstructed grain-boundary segments and the crystal orientations associated with them were used to compute subsets of the overall GBCDs, that is, the misorientation averaged grain-boundary plane distributions (GBPDs)^{20,26} and misorientation angle distributions (MADs).⁶⁵ The GBPD was determined using an in-house program.⁶⁶ The relative areas of all orientations were normalized to yield values based on multiples of a random distribution (MRD); in these units, values that differ from unity indicate orientations that have areas greater than or less than that expected in a uniform, isotropic distribution.^{20,26,32} Each stereological distribution was determined using at least 20 000 boundary segments to provide statistical significance to the GBPDs.²³

(3) Statistical Data Analysis

Dream.3D⁶⁷ was used to convert the processed EBSD data from a hexagonal (as measured) to a square grid, to obtain lists of grains, and to calculate their equivalent diameters. Grain size data were visualized using histograms and log-normal probability plots. To perform statistical analysis on the upper tails of GSDs, the POT method based on extreme value theory was used.⁵⁰ Three important parameters, the threshold, scale, and shape parameters, were calculated using the POT analysis to quantify the differences of upper tail departure.

To compare the experimental data to accepted models of grain growth, simulated GSDs were generated from several theoretical models. The Potts model (a Monte-Carlo grain growth method) is a standard isotropic grain growth model based on the probability of changes in grain-boundary orientation.^{59,68,69} A 2D Potts model⁶⁹ was used in the current investigation: the dataset was generated from a 1000² 2D grid. Distributions of random grain sizes that correspond to the Hillert⁵⁵ distribution and the Mullins⁵⁸ C distribution [Eq. 29 in Ref. (58)] were generated using inverse transform sampling. Inverse transform sampling involves inserting a random number along the interval [0,1] into the cumulative distribution function (cdf) of a probability distribution. The solution is a random sample from the underlying probability distribution function (pdf). If no closed form cdf exists for a given pdf, as is the case for the Mullins distribution, a discretized cdf can be generated by numerical integration of the pdf. This method allows for any number of random grain sizes to be generated numerically from any given pdf. The range of possible values of grain size is mediated by the interval chosen to discretize the cdf. The POT analysis was applied to these generated datasets and results were compared with the experimental datasets.

III. Results and Discussion

(1) IPF Maps and GSDs

IPF maps (with reconstructed grain-boundary segments) from representative regions are shown in Fig. 1 for (a) the dense 800 sample and (b) the porous AS sample. These IPF maps are representative of all the dense LSM samples. They illustrate that the EBSD data are well indexed, have clear

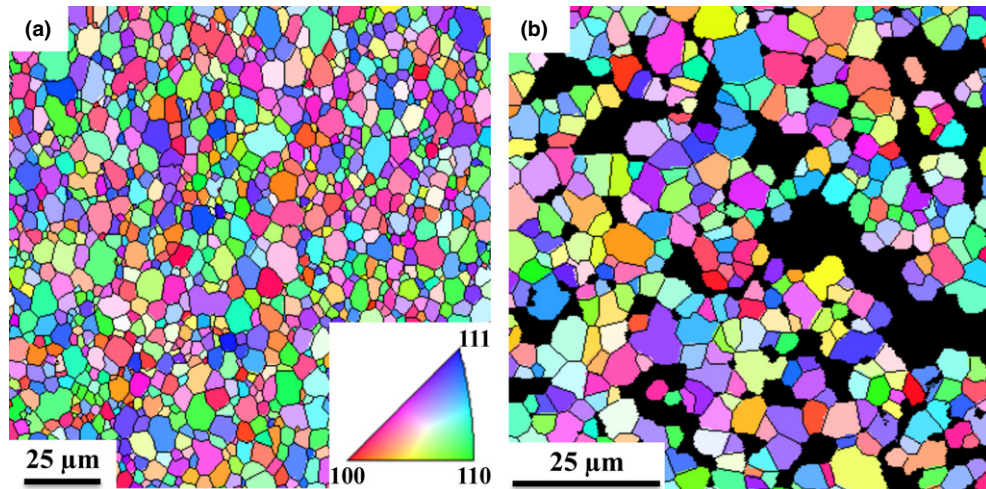


Fig. 1. Inverse pole figure map of a representative region of the (a) dense 800 sample and (b) porous AS sample. The data are cleaned and partitioned data with reconstructed boundaries. Note the different scales.

representations of grain-boundary line segments and grain sizes, and the porous network is captured throughout the data processing procedures. In all IPF maps, the grains were equiaxed. The porous LSM has a network of interconnected pores that is similar to that in an SOFC cathode.²²

The average grain size was $3 (\pm 1.5) \mu\text{m}$ for AS sample, which increased slightly to $4 (\pm 3) \mu\text{m}$ for the 1450 sample. The average grain size of the 800 and 1250 samples were $3 (\pm 2)$ and $4 (\pm 2) \mu\text{m}$, respectively. The average grain size for the porous AS sample is $3 (\pm 2) \mu\text{m}$, similar to the dense AS sample. The uncertainty in the average grain size (all calculations were performed using information from at least 12 000 grains) is large enough that this metric alone cannot distinguish samples.

The GSDs for all samples are shown in Fig. 2. All GSDs exhibit unimodal profiles. All curves have similar shapes and differ slightly in the locations of the individual GSDs along the x -axis. These similarities indicate that the postsintering thermal anneals have no qualitative effect on the GSD in dense LSM. The GSD for the porous AS sample is similar to the profile of the dense AS sample. The AS sample had the smallest (whereas the 1450 had the largest) average grain size and its GSD is to the leftmost of the others (whereas the 1450 is the rightmost), indicating the grain sizes are indeed slightly smaller for the AS sample than the other samples (and slightly larger for the 1450 sample). The GSDs of the 800 and 1250 samples are located between the GSDs of the AS and 1450 samples, and the GSD of the 1250 sample has

a slightly increased population of larger grains. According to the GSD plots, the most prevalent grain sizes for porous AS, dense AS, 800, 1250, and 1450 samples are 4, 5, 6, 6, and $8 \mu\text{m}$, respectively. (The average pore size measured is $3 (\pm 3) \mu\text{m}$, with many larger pores existing in the network.) The variations in the GSDs and grain sizes indicate the following: (1) thermal coarsening is active in the dense samples, although not extensive over the time scales investigated here, in all the annealing conditions, including the thermal conditions of SOFC operation; and (2) the types and quantities of pores introduced here had no obvious effect on the GSD of the AS sample.

(2) Interface Plane Distributions

To determine the relative anisotropy in these LSM-8020 ceramics, GBPDS of all dense LSM samples were calculated. The GBPDS are shown in Fig. 3 and exhibit a range in the relative areas between 0.87 and 1.16 MRD. This narrow range is indicative of extremely weak anisotropy, similar to YSZ,²³ especially by comparison to *fcc* metals³⁸ or other ceramics.^{26,32,34,39} Although the distributions are nearly isotropic, which would exhibit all orientations at an MRD value of 1, there is a weak increased (decreased) frequency of $\{001\}$ ($\{111\}$) planes in all samples. When the maxima and minima of the distributions from different samples differ by less than 10%, they are considered to be indistinguishable. In other words, all samples could be considered identical to one another, indicating the GBPDS had already reached steady state during the 4-h sintering period. The small increases in grain sizes do not result in a significant change in the GBPDS, as expected. These results indicate that LSM has almost isotropic GBPDS, which likely reflects nearly isotropic GBEDs, and that microstructural evolution in the dense compacts is driven largely by grain-boundary curvature and reduction in total area, as used in the recent SOFC evolution model.²⁴

The GBPDS of the porous AS sample is shown in Fig. 4(a). The sample also exhibits weak anisotropy, with a range of only 0.94–1.12 MRD, where $\{100\}$ ($\{111\}$) planes occur most (least) frequently. Overall, the GBPDS is slightly more isotropic as compared to the dense LSM sample. Because the average grain sizes and GSDs are similar between the porous and dense AS samples, the GBPDS could be considered to have reached steady state, so the slight narrowing likely indicates the pores render the GBPDS to be slightly more isotropic. What is interesting to notice is the PBSD [Fig. 4(b)] is opposite in shape to the GBPDS, with the slightly increased population in one being the slightly decreased population in the

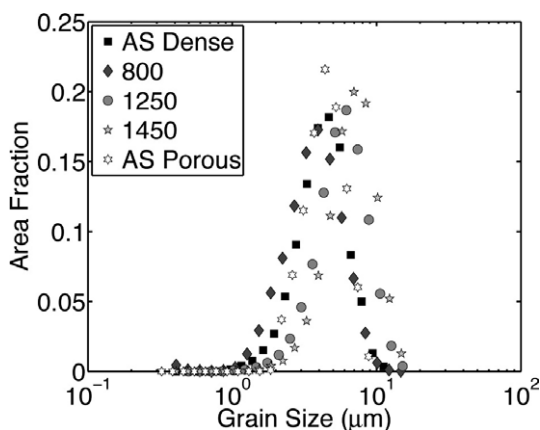


Fig. 2. Grain size distributions of all LSM samples: dense AS, 800, 1250, 1450, and porous AS.

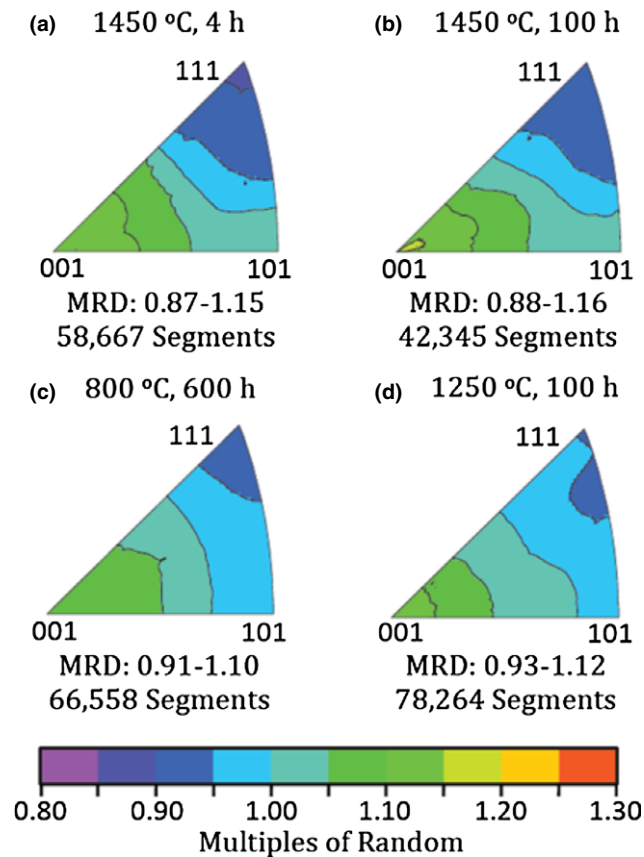


Fig. 3. Two-Dimensional grain-boundary plane distributions of dense LSM samples: (a) AS (b) 1450, (c) 800, and (d) 1250. MRD: multiples of a random distribution.

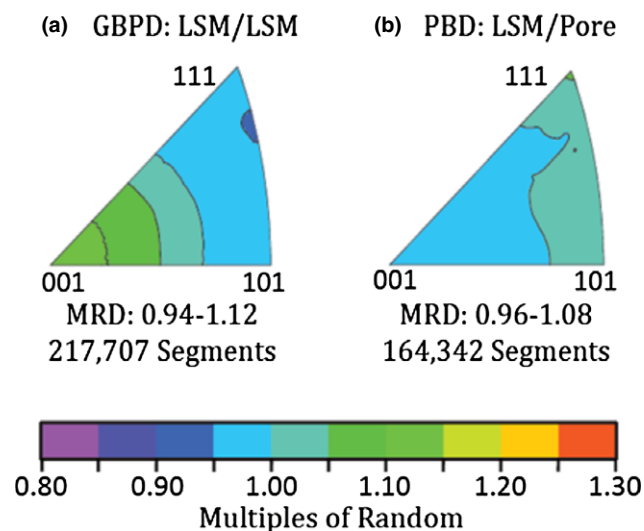


Fig. 4. Two-Dimensional grain-boundary plane distribution (a) and pore boundary plane distribution (b) for the porous AS sample. MRD: multiples of a random distribution.

other distribution. Whether this relation reflects independent energetic preferences or topological constraints on one distribution from the other, it is difficult to ascertain from this data because both distributions are nearly isotropic. However, these data clearly indicate that the crystallography of LSM surfaces span all orientations with nearly equal frequencies, even though the surface energy is anisotropic for LSM.^{70,71}

The observations given above indicate that LSM-8020: (1) arrives at steady-state GBPDs during the initial sintering, (2)

experiences a slight increase in grain size during further thermal treatments with little change in the shape of the GSDs, and (3) the GBPDs are amongst the most isotropic observed for polycrystalline systems.^{23,26,27,29,31–33,39,72,73} Interestingly, the microporous network introduced here had a minimal impact on those observations, and the PBDs are also essentially isotropic. These observations seem to imply that isotropic coarsening models should work well for this system and that the distributions should approach ideal behavior, and do not imply that pores have a significant influence. That the pores have an influence on the tails of the distribution was evinced by analyzing the tails of the distributions, focusing on how they deviate from log-normal behavior and how they compare to conventional models of coarsening.

(3) Probability Plots and POT Analysis of Upper Tails

(A) Probability Plots: The probability plots (plotted with R⁷⁴ statistical package) obtained from the model distributions are shown in Fig. 5. In probability plots, the x axis represents sample quantiles and the y axis scales percentiles

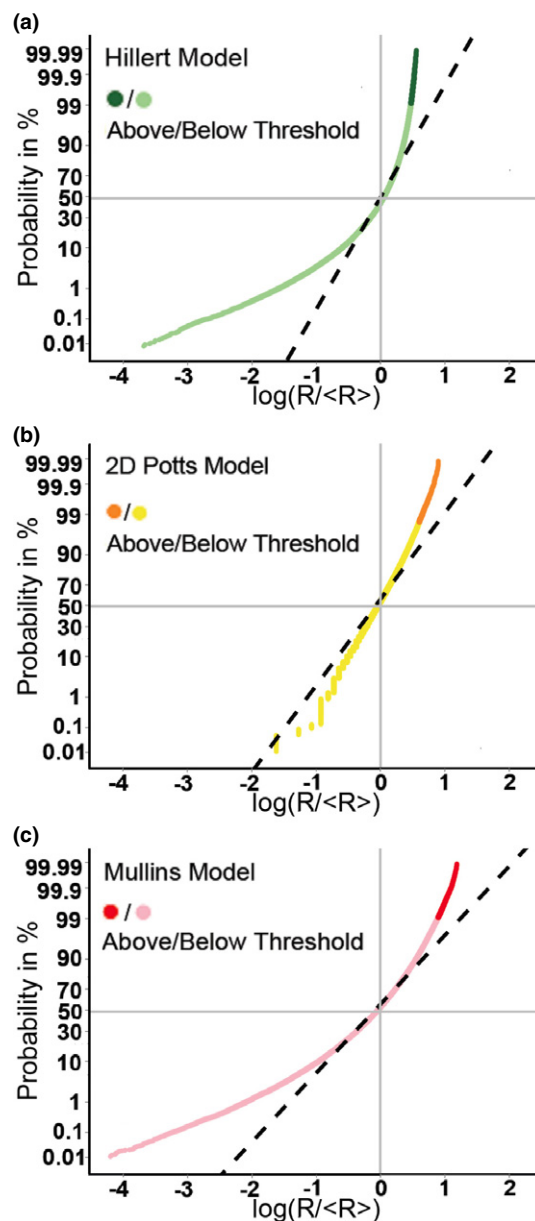


Fig. 5. Probability plots of normalized grain sizes from analytical grain growth models: (a) Hillert, (b) Potts, and (c) Mullins. The points above the threshold for POT analysis are differentiated.

of a theoretical distribution.⁵¹ The straight lines represent the expectation for a log-normal distribution: any distribution following log-normal behavior would superimpose on a straight line. The two shades (dark/light) in each probability plot indicate the values on different sides of the threshold value (above/below) determined in the POT analysis (discussed in the next section). Hillert's model has a cutoff of approximately two for normalized grain size (i.e., the largest normalized grain size is approximately twice the average size). On the probability plot, the Hillert distribution [Fig. 5(a)] deviates strongly from the log-normal distribution. For the 2D Potts (Monte-Carlo) model distributions [Fig. 5(b)], the deviation is less severe than the Hillert distribution, and the Mullins' distribution [Fig. 5(c)] exhibits the least severe deviation from the log-normal distribution. Both the Potts and Mullins distributions have infinite tails, that is, the largest normalized grain size could be infinite. Nevertheless, all have fewer large grains than expected from the log-normal distribution.

Figure 6 shows the probability plots for the five experimental datasets from LSM. The full distributions (again using two shades for each distribution) are shown in Fig. 6(a) for the dense AS, the 1250, and the porous AS samples. The upper tails (above the threshold) are shown in Fig. 6(b) for all the dense LSM samples, as well as for the Potts and Mullins models. Analysis of the upper tails reveals differences in grain growth at the various conditions of sintering and subsequent annealing, which are not evident from the histograms in Figs. 2 and 4. A negative tail departure from log-normal distribution is observed for the four dense LSM datasets, which are clustered together [Fig. 6(b)], whereas a positive tail departure is observed for the porous AS sample [Fig. 6(a)]. The negative tail departures indicate lower frequencies of large grains in the microstructure, which follows the trend observed for normal grain growth. In fact,

the experimental distributions are quite similar to the Mullins distribution [see Fig. 6(b)]. This corresponds well to expectations of nearly isotropic, dense materials observed in the equiaxed microstructures, GSDs, and GBPDs.

From this same point of view, the positive tail departure in the porous AS sample is surprising, as the earlier microstructural parameters were similar to those of the dense system. The positive tail departure indicates there are more large grains than expected in the log-normal distribution, and is consistent with the initial stages of abnormal grain growth where a small population of large grains grow faster than the rest of the distribution. Grain growth leading to abnormally large grains has been explained based on anisotropic natures of surface energies, grain-boundary energies, and grain-boundary mobilities.^{41,42} Interestingly, neither the isotropic nature of the GBPDs or PBPDs, nor the otherwise equiaxed microstructures implicate energy anisotropies as the likely cause of the positive tail departure. It is reasonable that grain-boundary mobilities differ between the two systems, as pores⁴⁰ and neck regions [see Ref. (44) and references therein] are known to affect boundary mobilities. Moreover, in ceramics with residual porosity, boundary depinning from pores is often a hallmark of abnormal grain growth [see Ref. (44) and references therein]. Brook⁴⁰ described grain growth in porous microstructures analytically, demonstrating that normal grain growth regularly changes to abnormal grain growth with the increase in grain size due to the pore-grain-boundary separation. The positive tail departure of the porous AS sample can be explained based on similar arguments. The larger grains in the tails of the porous structure indicate that, even in these almost isotropic systems (as indicated by the average GSD and the boundary distributions), heterogeneities exist that may impact performance or degradation, as the microstructure was shown above to slowly evolve even at the operation conditions.

(B) *POT Analysis of Upper Tails:* To quantify the differences in the upper tails, the POT analysis was used. The distribution function used for POT analysis is summarized as follows. The Generalized Extreme Value distribution⁷⁵ only provides information about the maximum variables. However, analysis of the whole range of values that constitute a distribution tail is preferred in reality.⁵⁰ To investigate the range of extreme values, a threshold (μ) was chosen above which variables can be considered as extreme values. The Pickands theorem⁷⁵ showed that the limiting distribution of normalized excesses of a μ is the Generalized Pareto Distribution (GPD). The three-parameter representation of the GPD is expressed with the following cdf:

$$G(x) = 1 - \left(1 + \xi \frac{x - \mu}{\sigma}\right)^{-\frac{1}{\xi}} \quad (1)$$

where μ , ξ , and σ are the location, shape, and scale parameters, respectively.

The threshold is equivalent to the location parameter of the GPD. A reasonable threshold selection is necessary for values in the tail to be well fit by the GPD. The POT package permits generation of several plots to choose the threshold value for each dataset. As in recent work, threshold choice plots and mean residual life plots were used to determine threshold values (μ) above which the modified scale (σ) and shape (ξ) parameters remain constant. The scale parameter reflects the spread of a probability distribution: a larger scale parameter will spread the entire probability density distribution. A negative shape parameter represents finite tail behavior, that is, fewer large grains. A positive shape parameter represents polynomial tail behavior, that is, more large grains. A shape parameter equal to zero corresponds to exponential tail behavior, which is expected in the log-normal distribution.⁵⁰

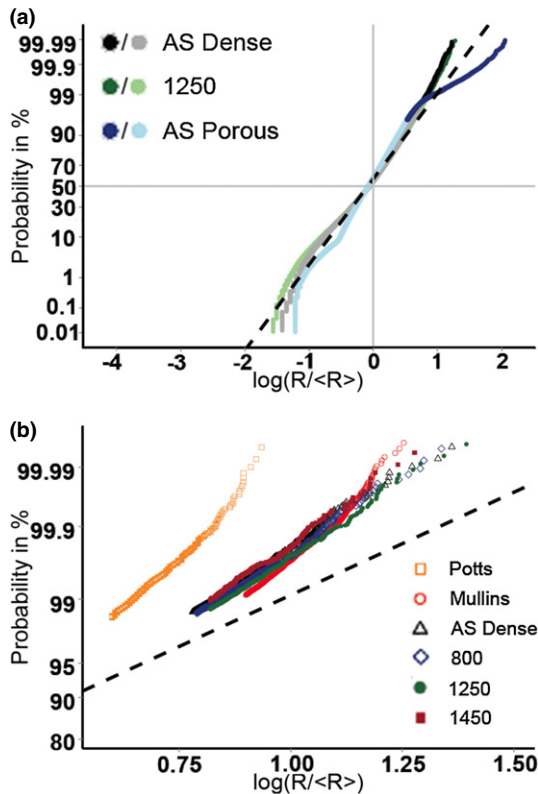


Fig. 6. Probability plots of normalized grain sizes from experimental LSM samples. (a) Full distributions for the dense AS, 1250, and porous AS, with the points above the threshold for POT analysis differentiated. (b) Upper tail of distributions (points above the threshold for POT analysis) for Potts and Mullins models, as well as all dense LSM samples.

Table I. POT Analysis of GSDs From Experimental Datasets and Theoretical Models, Given as Value (SD)

	AS porous	AS dense	800	1250	1450	Potts	Hillert	Mullins
μ (Threshold)	0.53	0.78	0.79	0.82	0.82	0.6	0.47	0.9
Scale parameter	0.2 (0.01)	0.14 (0.007)	0.14 (0.01)	0.13 (0.01)	0.11 (0.01)	0.1 (0.006)	0.03 (0.001)	0.11 (0.004)
Shape parameter	0.25 (0.03)	-0.16 (0.03)	-0.16 (0.02)	-0.14 (0.02)	-0.08 (0.01)	-0.2 (0.04)	-0.24 (0.03)	-0.19 (0.02)
Total Points	70 555	35 808	33 187	40 475	28 052	35 215	100 000	100 000
Points > μ	3209	513	491	538	294	591	853	894
Fraction > μ ($\times 10^{-2}$)	4.5	1.4	1.5	1.3	1.0	1.7	0.9	0.9

AS, as-sintered; GSD, grain size distribution; POT, peaks-over-threshold.

(C) *POT Observations:* The POT analysis results are presented in Table I. For POT analysis, each LSM sample dataset was divided into eight subsets to estimate the confidence level of the calculated parameters. The AS porous LSM sample has a positive shape parameter, which indicates that it has a longer tail as compared to log-normal distribution (as observed in Fig. 6). All dense LSM GSDs have negative shape parameters. Moreover, it is observed that the shape parameter values became slightly less negative with increasing annealing temperatures, from 800°C to 1450°C. The lengths of the upper tails for the dense LSM samples increased slightly with increasing annealing temperature.

To put these results in perspective, we can compare the experimental distributions to the theoretical ones. As mentioned above, the Hillert distribution is based on classical coarsening theory and exhibits the most negative shape parameter (corresponding to the shortest upper tail) among all GSDs; this corresponds to the hard cut-off of value of two for the normalized grain size. It also exhibited the lowest threshold. The Mullins distribution was designed to be closer to the experimental data available at the time, which did not show such a maximum grain size. Accordingly, it is reasonable that it and the Potts model have similar shape and scale parameters, and exhibited longer tails than exhibited by the Hillert distribution, but the Mullins and Potts model differ in their threshold value. All the LSM GSDs show longer tails than either the Hillert (theoretical) distribution, or the (numerical) Potts model, which indicates that none of the experimental systems are behaving in an ideal fashion. However, all the dense LSM distributions lie close to the Mullins distribution, which represents an empirically based choice from among the range of theoretically possible distributions. The main advantage of the POT analysis is the ability to quantify such differences as a complement to the visualization in the probability plots. Essentially, the Mullins distribution accurately captures the mean and upper tails in the dense samples, whereas the upper tails in the porous sample exhibit a low threshold value and large positive shape parameter, which is similar to what might be expected during the early stages of abnormal grain growth. The effect of pinning particles has already been observed to cause a deviation in the GSD upper tail from highly curved to straight, as observed on probability plots.^{50,76} The possible presence of abnormal grain growth could be explained based on the effect of pore boundary migration during microstructure evolution. This observation is interesting because it indicates the microscale pores in the microstructure of SOFCs perturb the tails of distributions (heterogeneities) that may evolve under operating conditions and may impact performance of SOFC electrodes.

IV. Conclusions

The crystallographic features of grain boundaries (GBCDs) and the grain size distributions were quantitatively characterized for LSM using EBSD data. The samples: (1) arrive at their steady state profiles for GBPDs and MADs during the initial sintering, (2) experience a slight increase in grain size during further thermal treatments, but exhibit little change in the normalized GSDs, (3) are among the most isotropic GBPDs observed for polycrystalline systems, and (4) exhibit a slightly increased (decreased) preference for {001} for the GBPDs (PBPDs). Log-normal probability plots of dense LSM show similar upper tail departures from log-normality, which are quite similar to the Mullin's distribution and which indicate there is nearly normal grain growth. The positive shape parameter for as-sintered porous LSM indicates a maximum frequency of large grains, as compared to all grain size distributions in this investigation, which could be explained based on the pore boundary migration being important during microstructure evolution.

Acknowledgments

The authors thank Kirk Gerdes (NETL) for useful discussions and encouragement. The project was performed in support of the National Energy Technology Laboratory's on-going research in Materials Science & Engineering: Solid Oxide Fuel Cell under the RDS contract DE-AC26-04NT41817. Authors also acknowledge support by the University Coal Research Program under Grant Number DE-FE0003840 from the Department of Energy as part of the University Coal Research Program. This work was partially supported by the Pennsylvania DCED.

References

- ¹N. Q. Minh and T. Takahashi, *Science and Technology of Ceramic Fuel Cells*. Elsevier, New York, 1995.
- ²A. Weber, R. Manner, R. Waser, and E. Ivers-Tiffée, "Interaction Between Microstructure and Electrical Properties of Screen Printed Cathodes in SOFC Single Cells," *Denki Kagaku*, **64** [6] 582–9 (1996).
- ³Y. C. Hsiao and J. R. Selman, "The Degradation of SOFC Electrodes," *Solid State Ionics*, **98** [1–2] 33–8 (1997).
- ⁴M. J. Jorgensen, P. Holtappels, and C. C. Appel, "Durability Test of SOFC Cathodes," *J. Applied Electrochemistry*, **30**, 411–8 (2000).
- ⁵S. P. Jiang and J. G. Love, "Observation of Structural Change Induced by Cathodic Polarization on (La,Sr)MnO₃ Electrodes of Solid Oxide Fuel Cells," *Solid State Ionics*, **158** [1–2] 45–53 (2003).
- ⁶A. Weber and E. Ivers-Tiffée, "Materials and Concepts for Solid Oxide Fuel Cells (SOFCs) in Stationary and Mobile Applications," *J. Power Sources*, **127** [1–2] 273–83 (2004).
- ⁷H. Y. Tu and U. Stimming, "Advances, Aging Mechanisms and Lifetime in Solid-Oxide Fuel Cells," *J. Power Sources*, **127** [1–2] 284–93 (2004).
- ⁸J. Desreux, Y. Bultel, L. Dessemond, and E. Siebert, "Theoretical Optimization of a SOFC Composite Cathode," *Electrochim. Acta*, **50** [10] 2037–46 (2005).
- ⁹S. P. Jiang and W. Wang, "Sintering and Grain Growth of (La,Sr)MnO₃ Electrodes of Solid Oxide Fuel Cells Under Polarization," *Solid State Ionics*, **176** [13–14] 1185–91 (2005).
- ¹⁰B. Butz, P. Kruse, H. Stormer, D. Gerthsen, A. Muller, A. Weber, and E. Ivers-Tiffée, "Correlation Between Microstructure and Degradation in Conductivity for Cubic Y₂O₃-Doped ZrO₂," *Solid State Ionics*, **177**, 3275–84 (2006).
- ¹¹H. Yokokawa, H. Tu, B. Iwanschütz, and A. Mai, "Fundamental Mechanisms Limiting Solid Oxide Fuel Cell Durability," *J. Power Sources*, **182** [2] 400–12 (2008).
- ¹²J. R. Wilson and S. A. Barnett, "Solid Oxide Fuel Cell Ni-YSZ Anodes: Effect of Composition on Microstructure and Performance," *Electrochim. Solid-State Lett.*, **11** [10] B181–5 (2008).
- ¹³S. Zhang, M. Lynch, A. M. Gokhale, and M. Liu, "Unbiased Characterization of Three-Phase Microstructure of Porous Lanthanum Doped Strontium Manganite/Yttria-Stabilized Zirconia Composite Cathodes for Solid Oxide Fuel Cells Using Atomic Force Microscopy and Stereology," *J. Power Sources*, **192** [2] 367–71 (2009).
- ¹⁴Y. L. Liu, K. Thyden, M. Chen, and A. Hagen, "Microstructure Degradation of LSM-YSZ Cathode in SOFCs Operated at Various Conditions," *Solid State Ionics*, **206**, 97–103 (2012).
- ¹⁵S. P. Jiang and W. Wang, "Sintering and Grain Growth of (La,Sr)MnO₃ Electrodes of Solid Oxide Fuel Cells Under Polarization," *Solid State Ionics*, **176**, 1185–91 (2005).
- ¹⁶D. Gostovic, J. R. Smith, D. P. Kundinger, K. S. Jones, and E. D. Wachsman, "Three-Dimensional Reconstruction of Porous LSCF Cathodes," *Electrochim. Solid St.*, **10** [12] B214–7 (2007).
- ¹⁷D. Gostovic, K. A. O'Hara, N. J. Vito, E. D. Wachsman, and K. S. Jones, "Multiple Length Scale Characterization of Doped Lanthanum Manganite Composite Cathodes," *ECSS Trans.*, **16**, 83–93 (2009).
- ¹⁸J. R. Wilson, J. S. Cronin, S. Rukes, A. Duong, D. Mumm, and S. Barnett, "Analysis of LSM-YSZ Composite Cathode Phase Connectivity Using Three-Dimensional Reconstructions," *ECSS Trans.*, **25** [2] 283–2292 (2009).
- ¹⁹J. R. Wilson, J. S. Cronin, A. T. Duong, S. Rukes, H. Y. Chen, K. Thornton, D. R. Mumm, and S. Barnett, "Effect of Composition of (La_{0.8}Sr_{0.2}MnO₃-Y₂O₃-Stabilized ZrO₂) Cathodes: Correlating Three-Dimensional Microstructure and Polarization Resistance," *J. Power Sources*, **195** [7] 1829–40 (2010).
- ²⁰T. Carraro, J. Joos, B. Ruger, A. Weber, and E. Ivers-Tiffée, "3D Finite Element Model for Reconstructing Mixed-Conducting Cathodes: I. Performance Quantification," *Electrochim. Acta*, **77**, 315–23 (2012).
- ²¹K. T. Lee, N. J. Vito, and E. D. Wachsman, "Comprehensive Quantification of Ni-Gd_{0.1}Ce_{0.9}O_{1.95} Anode Functional Layer Microstructures by Three-Dimensional Reconstruction Using a FIB/SEM Dual Beam System," *J. Power Sources*, **228**, 220–8 (2013).
- ²²S. Dillon, L. Helmick, H. Miller, L. Wilson, R. Gemman, R. Petrova, K. Barmak, G. S. Rohrer, and P. A. Salvador, "The Orientation Distributions of Lines, Surfaces, and Interfaces Around Three-Phase Boundaries in Solid Oxide Fuel Cell Cathodes," *J. Am. Ceram. Soc.*, **94** [11] 4045–51 (2011).
- ²³L. Helmick, S. J. Dillon, K. Gerdes, R. Gemmen, G. S. Rohrer, S. Seetharaman, and P. A. Salvador, "Crystallographic Characteristics of Grain Boundaries in Dense Yttria-Stabilized Zirconia," *Int. J. Appl. Ceram. Technol.*, **8** [5] 1218–28 (2011).
- ²⁴Q. Li, L. Y. Liang, K. Gerdes, and L. Q. Chen, "Phase-Field Modeling of Three-Phase Electrode Microstructures in Solid Oxide Fuel Cells," *Appl. Phys. Lett.*, **101** [3] 033909, 5pp (2012).
- ²⁵C. Goux, "Structure des Joints de Grains: Considérations Cristallographiques et Méthodes de Calcul des Structures," *Can. Metall. Q.*, **13** [1] 9–31 (1974).
- ²⁶D. M. Saylor, A. Morawiec, and G. S. Rohrer, "Distribution and Energies of Grain Boundaries in Magnesia as a Function of Five Degrees of Freedom," *J. Am. Ceram. Soc.*, **85** [12] 3081–3 (2002).
- ²⁷G. S. Rohrer, D. M. Saylor, B. E. Dasher, B. L. Adams, A. D. Rollett, and P. Wynblatt, "The Distribution of Internal Interfaces in Polycrystals," *Zeitschrift für Metallkunde*, **95**, 197–214 (2004).
- ²⁸D. M. Saylor, A. Morawiec, B. L. Adams, and G. S. Rohrer, "Misorientation Dependence of the Grain Boundary Energy in Magnesia," *Interface Sci.*, **8**, 131–40 (2000).
- ²⁹D. M. Saylor, A. Morawiec, and G. S. Rohrer, "The Relative Free Energies of Grain Boundaries in Magnesia as a Function of Five Macroscopic Parameters," *Acta Mater.*, **51** [13] 3675–86 (2003).
- ³⁰H. Miller, D. Saylor, B. E. Dasher, A. Rollett, and G. Rohrer, "Crystallographic Distribution of Internal Interfaces in Spinel Polycrystals," *Mater. Sci. Forum*, **467–470**, 783–8 (2004).
- ³¹D. M. Saylor, B. E. Dasher, Y. Pang, H. M. Miller, P. Wynblatt, A. D. Rollett, and G. S. Rohrer, "Habits of Grains in Dense Polycrystalline Solids," *J. Am. Ceram. Soc.*, **87** [4] 724–6 (2004).
- ³²D. M. Saylor, B. E. Dasher, T. Sano, and G. S. Rohrer, "Distribution of Grain Boundaries in SrTiO₃ as a Function of Five Macroscopic Parameters," *J. Am. Ceram. Soc.*, **87** [4] 670–6 (2004).
- ³³S. J. Dillon and G. S. Rohrer, "Three-Dimensional FIB-OIM of Ceramic Materials," *Ceram. Trans.*, **201**, 117–24 (2009).
- ³⁴S. J. Dillon and G. S. Rohrer, "Characterization of the Grain-Boundary Character and Energy Distributions of Yttria Using Automated Serial Sectioning and EBSD in the FIB," *J. Am. Ceram. Soc.*, **92** [7] 1580–5 (2009).
- ³⁵S. J. Dillon and G. S. Rohrer, "Mechanism for the Development of Anisotropic Grain Boundary Character Distributions During Normal Grain Growth," *Acta Mater.*, **57** [1] 1–7 (2008).
- ³⁶J. Gruber, D. C. George, A. P. Kuprat, G. S. Rohrer, and A. D. Rollett, "Effect of Anisotropic Grain Boundary Properties on Grain Boundary Plane Distributions During Grain Growth," *Scripta Mater.*, **53**, 351–5 (2005).
- ³⁷J. Gruber, H. M. Miller, T. D. Hoffmann, G. S. Rohrer, and A. D. Rollett, "Misorientation Texture Development During Grain Growth. Part I: Simulation and Experiment," *Acta Mater.*, **57** [20] 6102–12 (2009).
- ³⁸J. Li, S. J. Dillon, and G. S. Rohrer, "Relative Grain Boundary Area and Energy Distributions in Nickel," *Acta Mater.*, **57** [14] 4304–11 (2009).
- ³⁹G. S. Rohrer, "Grain Boundary Energy Anisotropy: A Review," *J. Mater. Sci.*, **46** [18] 5881–95 (2011).
- ⁴⁰R. J. Brook, "Pore-Grain Boundary Interactions and Grain Growth," *J. Am. Ceram. Soc.*, **52** [1] 56–7 (1969).
- ⁴¹C. V. Thompson, H. J. Frost, and F. Spaepen, "The Relative Rates of Secondary and Normal Grain-Growth," *Acta Metall. Mater.*, **35** [4] 887–90 (1987).
- ⁴²A. D. Rollett, D. J. Srolovitz, and M. P. Anderson, "Simulation and Theory of Abnormal Grain-Growth Anisotropic Grain-Boundary Energies and Mobilities," *Acta Metall. Mater.*, **37** [4] 1227–40 (1989).
- ⁴³F. J. Humphreys, "A Unified Theory of Recovery, Recrystallization and Grain Growth, Based on the Stability and Growth of Cellular Microstructures. 1. The Basic Model," *Acta Mater.*, **45** [10] 4231–40 (1997).
- ⁴⁴M. N. Rahaman, *Ceramic Processing and Sintering*, 2nd Edition. Marcel Dekker, Inc, New York, 2003.
- ⁴⁵E. Fjeldberg, E. Holm, A. D. Rollett, and K. Marthinsen, "Mobility Driven Abnormal Grain Growth in the Presence of Particles," *Mater. Sci. Forum*, **715–716**, 930–5 (2012).
- ⁴⁶K. Sasaki and J. Maier, "Chemical Surface Exchange of Oxygen on Y₂O₃-Stabilized ZrO₂," *Solid State Ionics*, **161** [1–2] 145–54 (2003).
- ⁴⁷L. Yan, K. R. Balasubramaniam, S. Wang, H. Du, and P. A. Salvador, "Effects of Crystallographic Orientation on the Oxygen Exchange Rate of La_{0.7}Sr_{0.3}MnO₃ Thin Films," *Solid State Ionics*, **194** [1] 9–16 (2011).
- ⁴⁸M. I. Mendelson, "Average Grain Size in Polycrystalline Ceramics," *J. Am. Ceram. Soc.*, **52** [8] 443–6 (1969).
- ⁴⁹M. F. Vaz and M. A. Fortes, "Grain-Size Distribution - the Lognormal and the Gamma-Distribution Functions," *Ser. Metall.*, **22** [1] 35–40 (1988).
- ⁵⁰S. P. Donegan, J. C. Tucker, A. D. Rollett, K. Barmak, and M. Groeber, "Extreme Value Analysis of Tail Departure From log-Normality in Experimental and Simulated Grain Size Distributions," *Acta Mater.*, **61** [15] 5595–604 (2013).
- ⁵¹J. C. Tucker, L. H. Chan, G. S. Rohrer, M. A. Groeber, and A. D. Rollett, "Tail Departure of Log-Normal Grain Size Distributions in Synthetic Three-Dimensional Microstructures," *Metall. Mater. Trans. A*, **43A** [8] 2810–22 (2012).
- ⁵²R. L. Coble, "A Model for Boundary Diffusion Controlled Creep in Polycrystalline Materials," *J. Appl. Phys.*, **34** [6] 1679–82 (1963).
- ⁵³K. O. Findley and A. Saxena, "Low Cycle Fatigue in Rene 88DT at 650 Degrees C: Crack Nucleation Mechanisms and Modeling," *Metall. Mater. Trans. A*, **37A** [5] 1469–75 (2006).
- ⁵⁴K. O. Findley, J. L. Evans, and A. Saxena, "A Critical Assessment of Fatigue Crack Nucleation and Growth Models for Ni- and Ni, Fe-Based Superalloys," *Int. Mater. Rev.*, **56** [1] 49–71 (2011).
- ⁵⁵M. Hillert, "On Theory of Normal and Abnormal Grain Growth," *Acta Metall. Mater.*, **13** [3] 227–38 (1965).

- ⁵⁶I. M. Lifshitz and V. V. Slyozov, "The Kinetics of Precipitation From Supersaturated Solid Solutions," *J. Phys. Chem. Solids*, **19** [1–2] 35–50 (1961).
- ⁵⁷C. Wagner, "Theorie Der Alterung Von Niederschlagen Durch Umlosen (Ostwald-Reifung)," *Z. Elektrochem.*, **65** [7–8] 581–91 (1961).
- ⁵⁸W. W. Mullins, "Grain Growth of Uniform Boundaries With Scaling," *Acta Mater.*, **46** [17] 6219–26 (1998).
- ⁵⁹R. B. Potts, "Some Generalized Order-Disorder Transformations," *P. Camb. Philos. Soc.*, **48** [1] 106–9 (1952).
- ⁶⁰S. J. Jiang, "Development of Lanthanum Strontium Manganite Perovskite Cathode Materials of Solid Oxide Fuel Cells: A Review," *J. Mater. Sci.*, **43**, 6799–833 (2008).
- ⁶¹R. E. Mistler and E. R. Twiname, *Tape Casting: Theory and Practice*. The American Ceramic Society, Westerville, 2000.
- ⁶²W. Schafbauer, N. H. Menzler, and H. P. Buchkremer, "Tape Casting of Anode Supports for Solid Oxide Fuel Cells at Forschungszentrum Jülich," *Int. J. Appl. Ceram. Technol.*, **11** [1] 125–35 (2014).
- ⁶³H. Moon, S. D. Kim, S. H. Hyun, and H. S. Kim, "Development of IT-SOFC Unit Cells With Anode-Supported Thin Electrolytes via Tape Casting and co-Firing," *Int. J. Hydrogen Energy*, **33** [6] 1758–68 (2008).
- ⁶⁴L. Helmick, "Microstructural Characterization of Solid Oxide Fuel Cell Cathode Materials," Ph.D. Thesis in Materials Science and Engineering, Carnegie Mellon University, Pittsburgh, (2010).
- ⁶⁵A. Morawiec, *Orientations and Rotations: Computations in Crystallographic Texture*. Springer, Berlin, 2004.
- ⁶⁶<http://mimp.materials.cmu.edu/~gr20/stereology/>.
- ⁶⁷<http://dream3d.bluequartz.net>.
- ⁶⁸A. Ayad, F. Wagner, N. Rouag, and A. D. Rollett, "Accelerated Potts Model for Grain Growth - Application to an IF Steel," *Comp. Mater. Sci.*, **68**, 189–97 (2013).
- ⁶⁹A. D. Rollett and P. Manohar, "Chapter 4: The Monte Carlo Method." pp. 77–14 in *Continuum Scale Simulation of Engineering Materials: Fundamentals-Microstructures-Process Applications*. Edited by D. Raabe, F. Roters, F. Barlat, and L.-Q. Chen. Wiley-VCH, Weinheim, 2004.
- ⁷⁰R. A. Evarestov, E. A. Kotomin, D. Fuks, J. Felsteiner, and J. Maier, "Ab Initio Calculations of the LaMnO₃ Surface Properties," *Appl. Surf. Sci.*, **238**, 457–63 (2004).
- ⁷¹R. A. Evarestov, E. A. Kotomin, Y. A. Mastrov, D. Gryaznov, E. Heifets, and J. Maier, "Comparative Density-Functional LCAO and Plane-Wave Calculations of LaMnO₃ Surfaces," *Physical Review B*, **72**, 214411, 12pp (2005).
- ⁷²A. D. Rollett, S. B. Lee, R. Campman, and G. S. Rohrer, "Three-Dimensional Characterization of Microstructure by Electron Back-Scatter Diffraction," *Annu. Rev. Mater. Res.*, **37**, 627–58 (2007).
- ⁷³C.-S. Kim, T. R. Massa, and G. S. Rohrer, "Modeling the Influence of Orientation Texture on the Strength of WC-Co Composites," *J. Am. Ceram. Soc.*, **90** [1] 199–204 (2007).
- ⁷⁴<http://www.r-project.org>.
- ⁷⁵M. Ribatet, A User's Guide to the POT Package (Version 1.4), 1–31 (2011). <http://www.cran.r-project.org/web/packages/POT/vignettes/POT.pdf>.
- ⁷⁶H. Li, S. Lee, and A. D. Rollett, "Study of the Effect of Pinning Particles on Grain Size Distributions," *Mater. Sci. Forum*, **753**, 361–7 (2013). □